Research Square

Preprints are preliminary reports that have not undergone peer review.
They should not be considered conclusive, used to inform clinical practice,
or referenced by the media as validated information.

Decoupling of the dynamic and subsurface thermal expressions of the climatological semiannual Rossby wave in the Bay of Bengal

Fuwen Qiu
Third Institute of Oceanography State Oceanic Administration: Third Institute of Oceanography Ministry of Natural Resources https://orcid.org/0000-0003-3552-7147
Wang Shucai
wangshucai@tio.org.cn
Third Institute of Oceanography Ministry of Natural Resources
Yun Qiu
Third Institute of Oceanography Ministry of Natural Resources
Junpeng Zhang
Third Institute of Oceanography Ministry of Natural Resources

Research Article

Keywords: Bay of Bengal, Semiannual Rossby wave, Sea level anomaly, Argo, Baroclinic modes

Posted Date: November 13th, 2026

DOI: https://doi.org/10.21203/rs.3.rs-11300434/v1

License: This work is licensed under a Creative Commons Attribution 4.0 International License.
Read Full License

Decoupling of the dynamic and subsurface thermal expressions of the climatological semiannual Rossby wave in the Bay of Bengal

Fuwen Qiu[1,2*] · Shucai Wang[1,2] · Yun Qiu[1,2,3,4] · Junpeng Zhang[1,2]

1 The Third Institute of Oceanography, Ministry of Natural Resources, Xiamen, China
2 Fujian Provincial Key Laboratory of Physical and Geological Processes, Xiamen, China
3 Southern Marine Science and Engineering Guangdong Laboratory (Zhuhai), Zhuhai, China
4 Laboratory for Regional Oceanography and Numerical Modeling, Qingdao National Laboratory for Marine Science and Technology, Qingdao, China

Abstract

The climatological semiannual Rossby wave of the Bay of Bengal is usually described from altimetric sea level anomaly (SLA) alone, on the assumption that sea level and subsurface temperature are interchangeable. We test this with 22 years (2004–2025) of altimetry and Argo data, using a plane-wave projection, a layer-wise steric decomposition and normal-mode solutions. Coherent westward propagation is confined to 7–11°N, 81–90°E, where direction purity exceeds 0.65. Only the subsurface thermal expression recovers a single freely propagating first-mode wave: the 160 m temperature, the 20°C isotherm depth and the 100–300 m steric height all give a wavelength near 18°, a speed of 12.6–12.9 cm s^{-1} and 0.97–0.98 of the variance explained by one plane wave. SLA is compressed to 11.8° and 8.3 cm s^{-1} and drifts in phase by up to 1.1 month, because part of the semiannual steric height is quasi-standing in the upper 100 m; removing that layer restores a 19.7° wave. The apparent amplitude decoupling is a normalization artifact: scaled with the observed thermocline displacement, the westward 160 m temperature component matches heaving to within 9%. Confining mode 1 to a 3° band reproduces the observed speed, whereas the two-dimensional mode is twice as fast, so the along-path speed variation in altimetry reflects interference rather than changing stratification. The winter–spring crest reaches the western boundary in February–April, deepening the thermocline by 10 m, while the summer–autumn event is cancelled by the annual cycle. A single altimetric view can misrepresent a baroclinic wave in a freshwater-influenced basin.

Keywords Bay of Bengal; Semiannual Rossby wave; Sea level anomaly; Argo; Baroclinic modes

1 Introduction

The Bay of Bengal (BoB) is a semi-enclosed tropical basin in the northeastern Indian Ocean whose upper-ocean circulation reverses almost completely with the seasonally reversing monsoon (Shankar et al. 2002; Schott et al. 2009). Its circulation, thermohaline structure and air–sea exchange are modulated by baroclinic waves that carry the signature of the equatorial Indian Ocean and of the basin's own boundaries into the interior (Shankar et al. 2002; Schott et al. 2009; Goswami et al. 2016; Chen et al. 2018). As one of the freshest tropical basins, the BoB receives enormous river discharge from the Ganges–Brahmaputra–Meghna and Irrawaddy systems and heavy monsoon rainfall, which together maintain a shallow, salinity-stratified surface layer and a barrier layer. Its upper-ocean steric

height and sea surface temperature are consequently unusually sensitive to air–sea fluxes rather than to thermocline motion (Vinayachandran et al. 2002; Han and McCreary 2001; Pang et al. 2024; Chen et al. 2025).

Among the basin-scale baroclinic signals of the BoB, the semiannual (180-day) component is particularly prominent. The monsoon winds contain a strong semiannual harmonic with two reversals per year, the equatorial Indian Ocean waveguide supports a vigorous semiannual response, and a 180-day wave needs about three months to cross the bay, so local and remote forcing can reinforce each other (Chen et al. 2025). Westward-propagating semiannual sea level signals driven by Ekman pumping have long been documented in the Indian Ocean (Masumoto and Meyers 1998). In the BoB the resulting semiannual reversal of the circulation is visible in the East India Coastal Current (EICC) (Shetye et al. 1993; McCreary et al. 1996) and in a band of high sea level anomaly (SLA) that propagates westward across the bay (Chelton and Schlax 1996; Somayajulu et al. 2003; Girishkumar et al. 2011).

Two independent observational windows are now available for describing this wave. Satellite altimetry measures the vertical integral of the density anomaly, that is the steric height, plus the mass contribution, and therefore resolves the dynamic expression of the wave at the sea surface. Profiling float arrays measure temperature and salinity, from which the thermal expression of the wave can be reconstructed at a fixed depth, most naturally in the thermocline where the vertical displacement of a baroclinic wave produces large temperature anomalies. The two windows are usually assumed to see the same wave, linked by heaving: the thermocline displacement ζ is taken to be linearly proportional to the sea level anomaly η, with a constant of proportionality given by the effective reduced gravity ratio g/g' of the stratification. Under that assumption the altimeter and the subsurface temperature are interchangeable measures of the wave (Gill 1982), which is why many studies describe the wave field from SLA alone.

The assumption has not been tested in the BoB, and there are three reasons to doubt it there. First, a large part of the steric height is generated in the upper 100 m, where temperature and salinity are controlled by air–sea fluxes rather than by thermocline motion (Vinayachandran et al. 2002; Han and McCreary 2001; Pang et al. 2024). Second, the semiannual period is close to the shortest period that a first-mode Rossby wave can attain at low latitudes, which makes its phase speed extremely sensitive both to the stratification and to the meridional structure of the wave (Gill 1982; Chelton et al. 1998; Killworth et al. 1997; Lin et al. 2008). Third, the climatological semiannual harmonic removes the interannual events that dominate visual inspection of SLA maps, leaving a low-amplitude, seasonally locked signal whose propagation is easily distorted by any standing component (Chelton and Schlax 1996; Somayajulu et al. 2003).

This paper therefore asks whether altimetric sea level and subsurface temperature resolve the same semiannual Rossby wave in the Bay of Bengal and, if they do not, which mechanism accounts for the difference. Three questions are addressed:

(i) How do the two observational windows differ in describing the wave, in amplitude, in zonal wavelength and in phase?

(ii) Why does the apparent propagation speed of the wave vary with longitude along its path?

(iii) What is the climatological significance of the wave, in particular for the circulation, for the subsurface temperature and salinity structure, and for the spring warm pool?

The analysis combines a harmonically filtered 22-year climatology of SLA and of Argo temperature and salinity in the 8–10°N band, a local plane-wave projection that separates the westward component from the standing and eastward components, a layer-wise decomposition of the steric height, an isotherm-based heaving test that does not rely on an assumed g/g′, and solutions of the vertical normal-mode problem for the observed stratification. Section 2 describes the data and methods, Section 3 the results, Section 4 the mechanisms and implications, and Section 5 the conclusions.

2 Data and methods

2.1 Data

Sea level. We use the monthly gridded sea level anomaly from the Copernicus/AVISO multimission DUACS L4 product (Pujol et al. 2016) on a 0.25° Mercator grid. The analysis window is 2004–2025 (264 months), the common period with the Argo product described below. We retain the region 79–96°E, 4–18°N, but compute all derivatives on an enlarged domain (73–101°E, 4°S–24°N) so that the ±4° zonal sliding window of the plane-wave projection is never truncated at the edges of the study region. The L4 product contains no explicit land mask in the coastal strip of the study region, so a land–sea mask based on the Natural Earth 1:10 m land polygons is applied before plotting, and all quantitative diagnostics are restricted to grid points with valid Argo data.

Temperature and salinity. We use the global monthly gridded Argo temperature and salinity product at 1° resolution with 58 standard levels between 2.5 and 1975 m (Argo 2000), constructed with the optimal-interpolation procedure of Roemmich and Gilson (2009) and covering January 2004 to February 2026. The diagnostics are based on the monthly climatology over 2004–2025. In the 8–10°N band between 80.5 and 90.5°E the 160 m temperature field is complete. Coverage degrades over the continental shelf and slope of the western boundary, where no valid profiles are available between 79.5 and 81.5°E north of about 12°N, and along the Andaman–Nicobar–Myanmar margin east of 91.5°E, so the northern and eastern margins of the maps are left blank rather than interpolated.

2.2 Harmonic decomposition

At every grid point the monthly climatology C(m), with m = 0,…,11 the month index, is decomposed into harmonics of the annual cycle. The semiannual component is written as $C_6(m) = A_6 \cos(2\pi m/6 - \varphi_6)$, and the amplitude A_6 and the peak month φ_6 are obtained by least squares from the 12 monthly values. On a 12-point annual cycle the 6-month and 12-month harmonics are orthogonal, so the annual cycle does not alias into the semiannual estimate; the annual harmonic is nevertheless fitted explicitly where it is needed, in Section 3.8. The residual left after removing the two harmonics contains the shorter periods (4 and 3 months) and any interannual contamination of the climatology, and is small, below 0.1°C at 160 m in the study band.

2.3 Local plane-wave projection

A harmonic amplitude alone does not distinguish a propagating wave from a standing oscillation. For every grid point along a given latitude we therefore project the semiannual component onto a set of plane waves $w(t,x) = \cos(2\pi t/6 - kx)$, where t is the month index, x the longitude in degrees and k the zonal wavenumber in rad deg^{-1}. The projection is performed in a zonal window of ±4° centred on the grid point, and a window is retained only if at least 80% of its members are valid. For each candidate k the explained variance is

$$EV(k) = [\ \Sigma_{t,x\in W}\ y\ w\ ]^2 / [\ (\ \Sigma_{t,x\in W}\ y^2\ )\ (\ \Sigma_{t,x\in W}\ w^2\ )\ ],$$

where y(t,x) is the reconstructed semiannual field of Section 2.2 and the sums run over the 12 months and over the valid longitudes of the window W. Scanning k gives the explained variance of the best westward wave, EV_W = max EV(k) over $k < 0$, and of the best eastward wave, EV_E = max EV(k) over $k > 0$, together with the corresponding optimal wavenumbers. The scan uses |k| from 0.04 to 0.95 rad deg^{-1} in steps of 0.01 for the westward branch and from 0.045 to 0.955 rad deg^{-1} for the eastward branch, corresponding to wavelengths from about 157° down to 6.6°.

Three quantities follow from the projection. The semiannual amplitude of the window is $A_6 = (2\langle y^2\rangle)^{1/2}$, with $\langle y^2\rangle$ the mean square of y over the window. The amplitudes of the two directional components are $A_{6W} = A_6\ (EV_W)^{1/2}$ and $A_{6E} = A_6\ (EV_E)^{1/2}$, that is, the part of the total amplitude that is carried by a wave propagating in each direction. The direction purity is

$$f_W = EV_W / (EV_W + EV_E),$$

so that $f_W = 1$ denotes a pure westward wave and $f_W = 0.5$ a standing or locally forced signal. Only points with $f_W \geq 0.65$ are interpreted as free westward propagation; elsewhere the phase slope of the total field has no wave interpretation, a distinction that is essential for question (ii). The zonal wavelength of the westward component follows from the optimal k as $\lambda = 2\pi/|k|$. Before the projection the monthly climatology is smoothed in latitude with a three-point running mean, which removes grid-scale noise without shifting the position of the coherent band.

2.4 Decoupling diagnostics

Two indices quantify the difference between the altimetric and the thermal expressions.

The amplitude ratio, $\Gamma = A_{6W}(T_{160}) / [A_{6W}(SLA) \cdot (g/g') \cdot |\partial T/\partial z|_{160}]$, compares the measured amplitude of the westward 160 m temperature component with the amplitude predicted by pure heaving, using a fixed two-layer reduced-gravity conversion $g/g' = 490$, obtained from $g = 9.81$ m s^{-2} and $g' = 0.02$ m s^{-2}, equivalent to $\Delta\rho/\rho \approx 2 \times 10^{-3}$, and the local climatological vertical temperature gradient $|\partial T/\partial z|_{160}$, computed by centred differencing of the climatological profile between the two Argo levels that bracket 160 m. A value $\Gamma = 1$ denotes pure heaving.

The phase difference $\Delta\varphi$ is the peak month of the 160 m temperature minus that of SLA, expressed in months and reduced to the interval (−3, +3]. Positive values mean that the subsurface thermal signal lags the dynamic signal, and $\Delta\varphi = 0$ is expected for pure heaving. Unlike Γ, the phase difference contains no free parameter.

2.5 Heaving test based on the observed thermocline displacement

Because g/g′ is not known a priori in the BoB, we also perform a heaving test that uses only observed quantities. Working with the 8–10°N band-mean profiles, we compute for each longitude the monthly climatology of the depth

of the 20°C isotherm, D_{20}, by linear interpolation of the Argo temperature profile, and fit its semiannual harmonic to obtain an amplitude A_{D20} and a peak month. The temperature anomaly at 160 m predicted by heaving is then $A_{D20}|\partial T/\partial z|_{160}$, with the gradient taken from the same band-mean profile, and we define

$$\Gamma_{obs} = A_{6W}(T_{160}) / [A_{D20} \cdot |\partial T/\partial z|_{160}],$$

where $A_{6W}(T_{160})$ is the westward-component amplitude of the band-mean 160 m temperature (Section 2.3). We also report the observed displacement-to-height ratio $\zeta/\eta = A_{D20}/A_{6W}(\mathrm{SLA})$, where $A_{6W}(\mathrm{SLA})$ is the westward-component amplitude of the band-mean SLA, which can be compared with the value predicted by the first baroclinic mode. All indices of this section and of Section 2.4 are formed on the same westward-component amplitudes, so they share a common normalization: Γ is evaluated pointwise on the A_{6W} fields, whereas Γ_{obs} and ζ/η use the band-mean A_{6W} amplitudes together with the band-mean D_{20} displacement. The three indices differ only in how sea level is converted into a displacement, which is either assumed (g/g') or observed (A_{D20}).

2.6 Layer-wise steric decomposition

To identify which part of the water column generates the altimetric signal, we compute the semiannual steric height anomaly from the Argo monthly climatology as $\eta_{ster}(z_1,z_2) = -\int_{z_1}^{z_2} (\Delta\rho/\rho_0)\, dz$, with $\rho_0 = 1025$ kg m^{-3} and $\Delta\rho$ the monthly density anomaly relative to the annual mean, computed with the UNESCO EOS-80 equation of state (UNESCO 1981) at the in-situ pressure. The layers examined are 0–50 m, 50–100 m, 100–200 m, 0–100 m, 0–200 m, 0–300 m, 200–1000 m and 0–1900 m. For each layer we fit the semiannual harmonic and compare its amplitude, its wavelength and its phase with those of the altimetric SLA.

2.7 Vertical normal modes and the theoretical semiannual Rossby wave speed

For each longitude in the 8–10°N band we compute the buoyancy frequency from the annual-mean Argo temperature and salinity profiles as $N^2 = (g/\rho_0)\partial\rho/\partial z - g^2/c_s^2$, with $\rho_0 = 1025$ kg m^{-3}; the second term removes the adiabatic compressibility contribution, with ρ from EOS-80 and the sound speed c_s from Mackenzie (1981). We then solve the standard vertical mode problem

$$d/dz[(1/N^2)\, d\Psi_n/dz] + \Psi_n/c_n^2 = 0, \;\; d\Psi_n/dz = 0 \text{ at } z = 0 \text{ and } z = -H,$$

on a 2 m grid with H = 2500 m, using a symmetric finite-difference discretization; the mode speeds follow from the eigenvalues μ_n as $c_n = (-\mu_n)^{-1/2}$. The scheme was verified against the analytic two-layer solution: for a synthetic profile with $g' = 0.02$ m s^{-2} and $H_1 = 100$ m the numerical and analytic mode-1 speeds agree to 0.7%, and the ratio of interface displacement to surface elevation agrees with g/g' to within 1%. From the modes we also obtain the vertical displacement structure (Chelton et al. 1998),

$$R_n(z) = |\zeta_n(z)/\eta_n| = |g\, \Psi'_n(z) / (N^2(z)\, \Psi_n(0))|,$$

which gives the heaving amplitude at any depth for a given sea surface height and hence a theoretical prediction of $\Gamma(z)$. Finally, the phase speed of a semiannual Rossby wave of mode n is obtained from the dispersion relation $\omega = -\beta k/(k^2 + l^2 + f^2/c_n^2)$, written as a quadratic in k and solved for the long-wave root,

$$k = [\, -\beta/\omega + (\beta^2/\omega^2 - 4(l^2 + f^2/c_n^2))^{1/2} \,] / 2,$$

with $\omega = 2\pi/(180\ \text{days})$, β and f evaluated at 9°N, and the meridional wavenumber either $l = 0$ or $l = \pi/L_y$ for a wave confined to a band of meridional width L_y. The wavelength follows from the root as $2\pi/|k|$ and the phase speed as $\omega/|k|$.

3 Results

3.1 Where the semiannual wave is coherent

Figure 1 maps the westward semiannual component in the bay. The amplitude of the SLA component (Fig. 1a) has a broad maximum between the equator and 5°N and a secondary maximum in the eastern bay near 10–14°N, 90–95°E, with amplitudes of 3–5 cm. The 160 m temperature component (Fig. 1b) reaches 0.6–0.9°C in the central and eastern bay between 6 and 12°N. Direction purity, with stippling marking $f_W < 0.65$, shows that the semiannual signal is predominantly standing or locally forced in the southern and northern bay, whereas a well-defined westward band extends from the western boundary to 93°E between about 7 and 11°N, centred on 8–10°N (Fig. 2a). In that band f_W reaches 0.93 for SLA and 0.84 for the 160 m temperature. For comparison, f_W is only 0.47–0.52 in the upper 50 m (Fig. 2d), where the semiannual temperature signal is controlled by surface fluxes rather than by thermocline motion. We therefore focus the rest of the analysis on the 8–10°N band, and within it on 81–90°E, the longitude range where both fields are coherent.

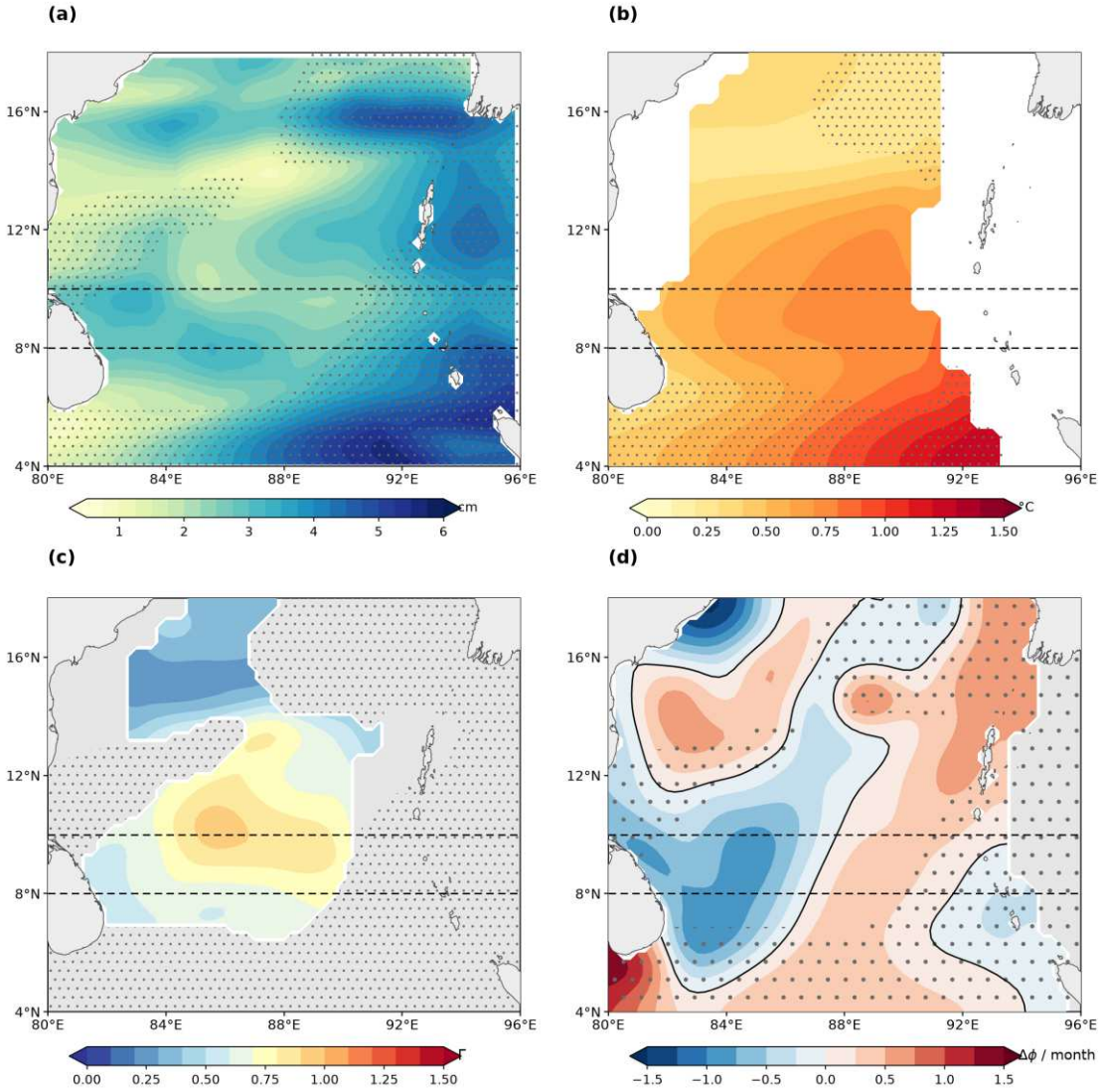


Fig. 1 Spatial structure of the semiannual (180-day) westward component in the Bay of Bengal, 2004–2025. (a) Amplitude A_{6W} of SLA (cm). (b) A_{6W} of the 160 m temperature (°C). (c) Amplitude ratio Γ with $g/g' = 490$. (d) Phase difference Δφ between the 160 m temperature and SLA (month). In all panels the westward component is isolated with a ±4° local plane-wave projection; stippling marks $f_W < 0.65$, where the semiannual signal is standing or locally forced and cannot be interpreted as free propagation. Light grey in (c) and (d) marks grid points where the diagnostics are undefined, because of data voids or $f_W < 0.65$. The two horizontal dashed lines delimit the 8–10°N band used throughout this paper. White areas are data voids, where no valid Argo profiles exist

3.2 Amplitude and phase of the two expressions

Along 8–10°N the amplitude of the westward SLA component increases from 2.29 cm at 79.5°E to 3.14 cm at 82.5°E, decreases to a local minimum of 2.40 cm at 88.5–89.5°E, and increases again to 3.92 cm at 94.5°E (Figs. 1a, 2c). The 160 m temperature amplitude increases monotonically eastward from 0.41°C at 79.5°E to 0.75°C at 89.5°E (Fig. 1b). The two amplitude distributions are therefore out of step, with SLA peaking in the west and temperature in the east.

The amplitude ratio Γ computed with g/g′ = 490 (Fig. 1c) is below unity everywhere in the band, ranging from 0.54 at 81.5°E to 0.94 at 85.5°E, with a band mean of about 0.74. Taken at face value this would imply that the 160 m thermal signal is one quarter weaker than the heaving prediction; Section 3.5 shows that it is instead an artifact of the assumed conversion factor.

The phase difference Δφ (Fig. 1d) is positive in the east, +0.39 to +0.46 month between 88 and 90.5°E, and negative in the west, decreasing to −0.51 month at 82.5°E and −1.13 month at 81.5°E. The zero crossing lies near 87°E. Along the propagation path the subsurface thermal signal thus changes from lagging sea level by about two weeks in the east to leading it by two to five weeks in the west. For a single wave obeying pure heaving Δφ would vanish everywhere; the drift is monotonic and matches the difference in zonal wavelength derived below, so it cannot be attributed to noise.

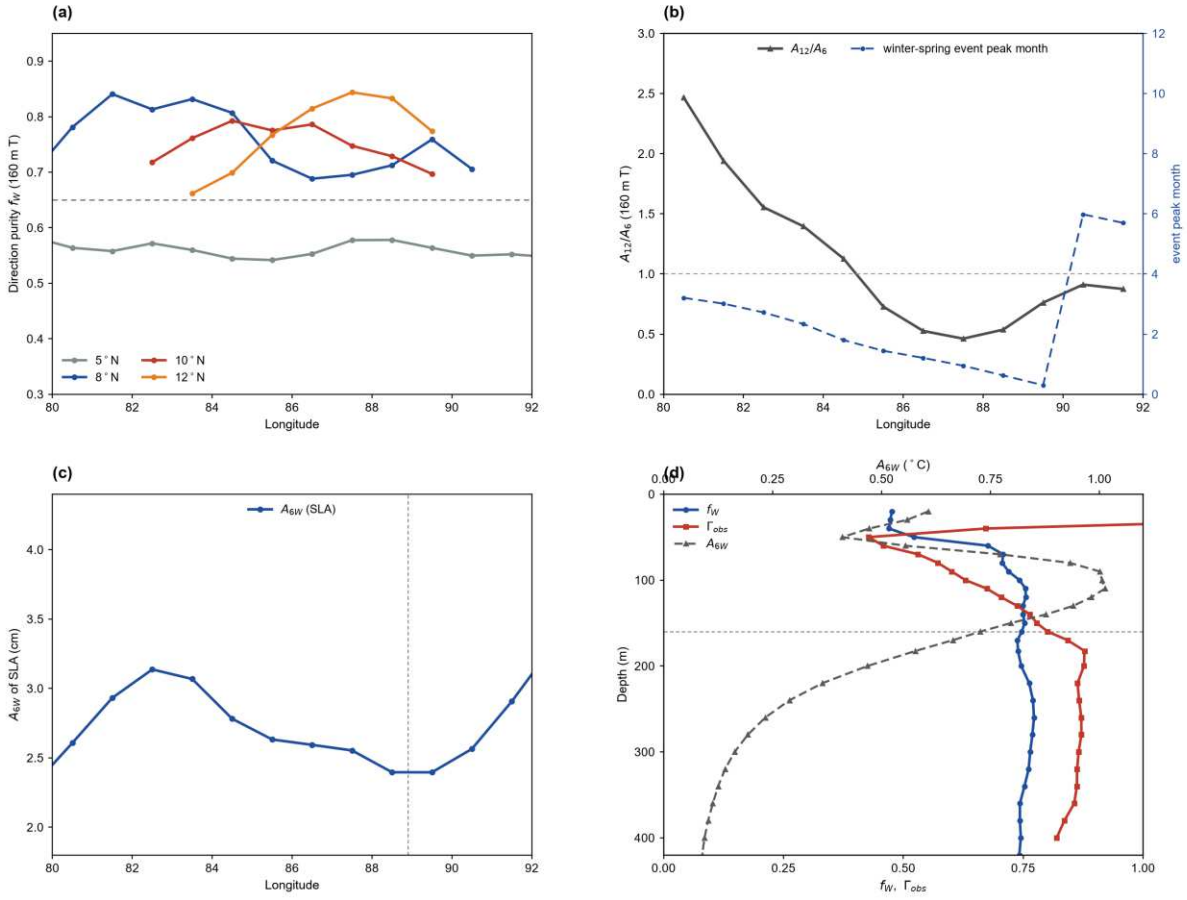


Fig. 2 Supporting diagnostics along 8–10°N. (a) Direction purity f_W of the semiannual signal at 5, 8, 10 and 12°N, showing that the 8–10°N band is the most coherent westward-expressing latitude. (b) Ratio of the annual to the semiannual harmonic amplitude (left axis) and the winter–spring event peak month (right axis). (c) Amplitude of the westward SLA component. (d) Depth dependence of the direction purity f_W, of the semiannual amplitude A_{6W}, of the heaving ratio Γ_{obs} and of the winter–spring event amplitude A_{SW}

3.3 The two expressions have different zonal wavelengths

Figure 3 shows the 8–10°N band-mean longitude–time sections of the raw monthly anomaly (Fig. 3a, b) and of the semiannual component (Fig. 3c, d). Both semiannual sections show the characteristic westward tilt and are phase-locked to the calendar year: the crests recur in the same months in successive years, so the signal forms part of the deterministic annual cycle rather than a sequence of independent events. The amplitudes of the individual events and the phase difference derived from these sections are quantified in Figs. 4a and 5c.

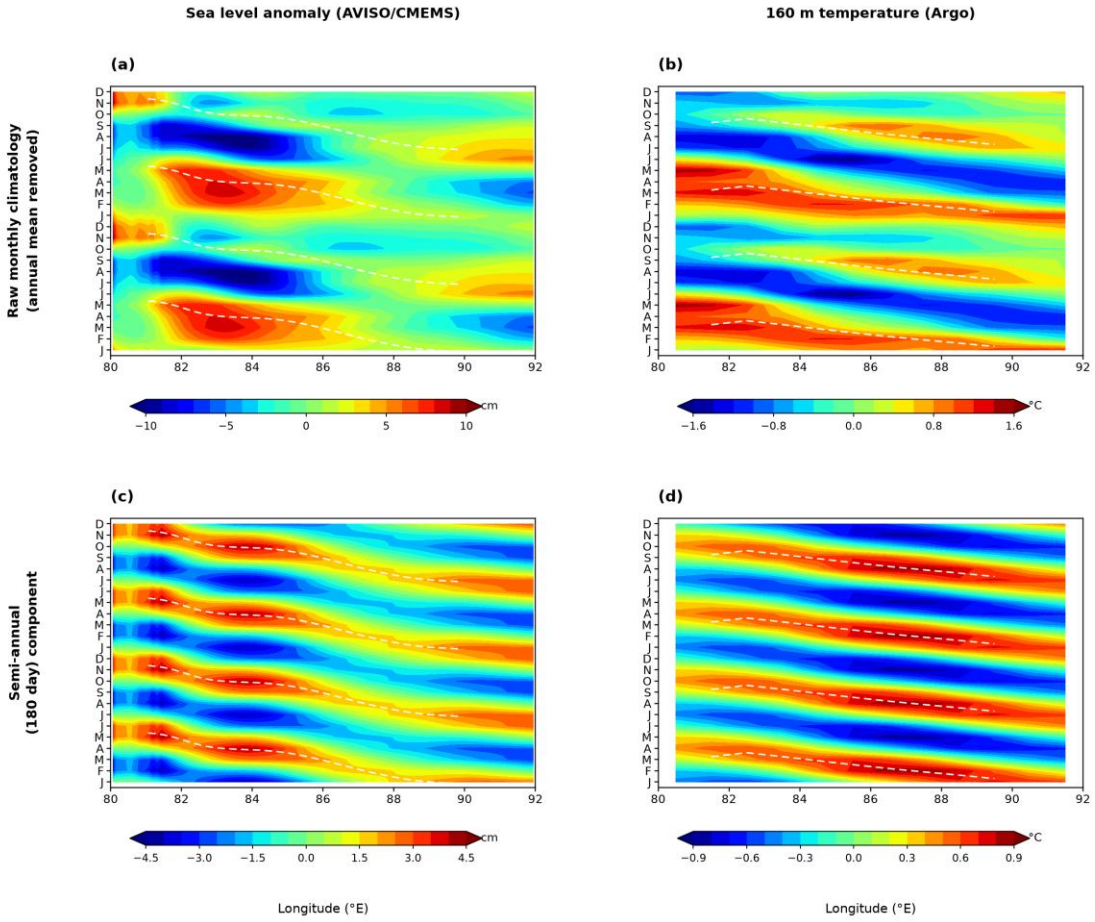


Fig. 3 Longitude–time sections of the 8–10°N band-mean fields. Rows: raw monthly climatological anomaly with the annual mean removed (a, b) and the semiannual (180-day) component (c, d). Columns: SLA (left, cm) and 160 m temperature (right, °C). White dashed lines in all panels are the unwrapped peak-month ridges, drawn between 81 and 90°E. The time axis runs upward over 24 months with single-letter month labels, so that a westward-propagating signal appears as stripes tilting from upper left to lower right

The zonal phase gradients are quantified in Fig. 4a, where the unwrapped semiannual peak month is plotted against longitude for several fields. Between 81.5 and 90.5°E the SLA phase decreases by 4.5 months, giving a zonal wavelength of 12.0°, about 1320 km, and a westward phase speed of 8.5 cm s^{-1}; the single-plane-wave fit of Section 3.4 returns 11.8° and 8.3 cm s^{-1}, so the two estimates agree to within 3%. Over the same longitude range the 160 m temperature phase decreases by only 3.0 months, giving 17.8° (about 1980 km) and 12.6 cm s^{-1} from the phase regression and 18.0° and 12.6 cm s^{-1} from the plane-wave fit. The depth of the 20°C isotherm gives 18.3° and 12.9 cm s^{-1}, and the steric height of the 100–200 m layer gives 18.0° and 12.8 cm s^{-1}. A single plane wave fitted to the 160 m temperature over the same range explains 97% of the variance, so the thermal field is close to one plane wave.

The 35% difference in wavelength between the two fields is therefore not a fitting artifact. It is the kinematic expression of the phase drift in Fig. 1d, since a phase difference growing westward at the rate $\partial\Delta\varphi/\partial x = 1/\lambda_{SLA} - 1/\lambda_T$ reproduces the observed drift of about 1.5 months across 81–90°E quantitatively.

3.4 A quasi-standing near-surface component in the altimetric signal

Figure 4b decomposes the semiannual steric height anomaly into layers. Averaged over 81.5–90.5°E the total steric height anomaly integrated over 0–1900 m is 3.05 cm, that is 108% of the mean SLA amplitude of 2.83 cm, so the semiannual SLA is essentially steric, as expected. The vertical distribution is, however, highly non-uniform: the 0–50 m layer contributes 1.34 cm, 47% of the SLA amplitude, the 50–100 m layer 1.25 cm, the 100–200 m layer 1.97 cm (70%), and the 200–1000 m layer 1.27 cm. Because the layers are not in phase these amplitudes do not add linearly, and the 0–200 m integral reaches 2.81 cm, essentially the whole SLA.

The key result is the behavior of the phase. Fitting the complex semiannual amplitude of each layer with a single zonal plane wave $C(x) = A\, e^{ikx}$ over 81–91°E gives the following results. The 0–50 m steric anomaly has a wavelength of about 90° over 81–91°E ($k = 0.070$ rad deg^{-1}, explained variance 0.96); fitted over the wider range shown in Fig. 4a the estimate is 117°, which confirms how weak the zonal phase gradient is: its peak month varies by less than half a month across the bay, so it is quasi-standing. The 0–100 m integral behaves in the same way but less purely, with 43–52° and an explained variance of 0.77. In contrast, the 100–200 m and the 100–300 m layers both propagate westward with 18.0° ($k = 0.350$ rad deg^{-1}) and 12.8 cm s^{-1}, with explained variances of 0.98; these values are statistically indistinguishable from those of the 160 m temperature ($k = 0.350$ rad deg^{-1}, 18.0°, 0.97) and of the 20°C isotherm depth (18.3°). The thermocline steric height and the subsurface thermal expression are therefore one and the same wave. Removing the upper layer from the water column, that is forming the 100–1900 m steric height as the difference between the 0–1900 m and the 0–100 m complex amplitudes, restores a clean 19.7° wave with an explained variance of 0.99. The total 0–1900 m steric height, which contains both, has an intermediate wavelength of 15.6° (11.0 cm s^{-1}).

The steric height at the sea surface is therefore the sum of a quasi-standing signal generated in the upper 100 m and of a westward-propagating thermocline signal. Superposing two coherent components of different wavenumber makes the phase of the sum rotate faster than that of either component where the two are nearly out of phase. This is why the wavelength of the total steric height, 15.6°, is shorter than that of the propagating thermocline component, 19.7°, instead of lying between the two, and why the amplitude must reach a minimum near the longitude where the two components cancel. Both features appear in the altimetric field at 88–89°E (Fig. 1a, d): the SLA amplitude drops to 2.40 cm, its lowest value between 81 and 92°E, and $\Delta\varphi$ jumps from −0.35 month at 86.5°E to +0.46 month at 88.5°E. At that longitude the direction purity of SLA is still $f_W = 0.73$–0.83, so the amplitude minimum is not a standing-wave node but the result of interference between two coherent components.

The superposition explains the compression from 19.7° to 15.6° but not the whole of the difference between SLA and the thermocline: the observed SLA wavelength is 11.8°, and in the complex-amplitude domain SLA differs from the 0–1900 m steric height by 52% of its amplitude, which is far larger than the difference between the two steric integrals themselves. Two readings are possible. Either the semiannual SLA contains a substantial non-steric

contribution, a mass or barotropic component with a different zonal structure, or the 0–1900 m steric estimate misses part of the signal, for example below 1900 m. Our data cannot separate the two, and we therefore do not claim that the steric decomposition explains the altimetric wavelength completely. What is robust is the ordering: the subsurface thermal expression and the thermocline steric height share one wavenumber, $k = 0.350$ rad deg^{-1} with an explained variance above 0.98, the sea surface does not share it, and no superposition of a quasi-standing component with the thermocline wave can produce the observed sea-surface wavenumber on its own.

3.5 The subsurface thermal signal is consistent with thermocline heaving

Figure 4c shows the semiannual amplitude of D_{20}, which averages 9.5 m over 81–90°E, with individual values between 5.9 and 11.0 m over the wider 80–92°E window. Figure 4d compares two estimates of the amplitude relation. The conventional index Γ, computed with $g/g' = 490$, is 0.54–0.94 with a band mean of about 0.74. The isotherm-based index Γ_{obs}, which uses the observed D_{20} displacement instead of an assumed conversion factor, is 0.90–1.24 with a band mean of 1.01 over 82.5–89.5°E, rising to 1.54 at 90.5°E where the wave amplitude decays. The measured 160 m temperature anomaly therefore follows the heaving prediction based on the observed thermocline: the two agree to within 9% on average across the band, and the deviation exceeds 20% only at the two easternmost longitudes.

The discrepancy between the two indices is a question of normalization. The displacement-to-height ratio $\zeta/\eta = A_{D20}/A_{6W}(\mathrm{SLA})$, evaluated at each longitude, averages 370 along the band, with a range of 283–435 over 82.5–90.5°E; for reference, the ratio of the band-mean amplitudes is 9.5 m / 2.64 cm ≈ 359, the along-band mean of the ratios being raised by the low-SLA longitudes near the interference minimum discussed in Section 3.4. The two-layer value $g/g' = 490$ used in Γ is larger still, whereas the first baroclinic mode of the local stratification predicts $R_1(115\ \mathrm{m}) \approx 165$ at the mean D_{20} depth. The observed ratio thus lies between the mode-1 prediction and the two-layer value. It lies above the mode-1 prediction because the westward SLA component is reduced by the partial cancellation with the quasi-standing surface layer discussed in Section 3.4: the sea level signal dynamically associated with the thermocline displacement is larger than the observed total SLA. Because these indices are formed at each longitude before averaging, they should be read as orderings rather than combined algebraically; the ordering is unambiguous, and it is the ordering that carries the interpretation.

We conclude that the subsurface thermal expression is a faithful measure of the thermocline displacement of the wave, and that the apparent amplitude decoupling in Fig. 1c is largely a consequence of the choice of conversion factor. What remains genuinely decoupled is the kinematics: the surface and subsurface expressions do not share a single wavelength.

3.6 Theoretical wave speed and the origin of the along-path speed variation

Figure 4a also allows a test of the dynamics. From the Argo annual-mean stratification the first baroclinic mode speed is $c_1 = 2.42$–2.54 m s^{-1}, corresponding to a deformation radius $L_{d1} = 106$–111 km at 9°N, and the second mode gives $c_2 = 1.51$–1.57 m s^{-1} ($L_{d2} = 66$–69 km); both vary by less than 4% along 80–92°E. A semiannual first-mode Rossby wave under these conditions would travel at 26.0 cm s^{-1} with a wavelength of 4100 km in the classical two-

dimensional limit $l = 0$, which is twice the observed thermocline speed. The semiannual wave in the bay is, however, confined to a band only a few degrees wide (Section 3.1), and for a wave confined to a meridional width L_y the meridional wavenumber $l = \pi/L_y$ enters the dispersion relation quadratically. With $L_y = 3°$ (330 km), l^2 is comparable to f^2/c_1^2 and the mode-1 speed falls to 12.3 cm s^{-1} with a wavelength of 1940 km, in close agreement with the observed thermocline values of 12.6–12.9 cm s^{-1} and 1980–2040 km. With $L_y = 4°$ the predicted speed is 16.1 cm s^{-1}, so the observations constrain the effective meridional width of the wave to about 3° (Killworth et al. 1997).

3.7 Depth dependence and the choice of the 160 m reference level

Figure 2d collects the diagnostics that were used to choose the reference depth. The direction purity f_W of the semiannual temperature signal increases from 0.47–0.52 in the upper 50 m to 0.71–0.76 between 70 and 120 m, and remains at 0.74–0.77 down to 400 m. The semiannual amplitude peaks at 1.03°C near 90–100 m, where $|\partial T/\partial z|$ is largest at 0.126°C m^{-1}, and decreases to 0.75°C at 160 m and 0.48°C at 200 m. The isotherm-based heaving ratio Γ_{obs} is close to unity at 160 m and above. A depth of 160 m is therefore a good compromise: the signal lies on the f_W plateau, the gradient $|\partial T/\partial z| = 0.069$°C m^{-1} still converts a few metres of displacement into a detectable temperature anomaly, and the level lies below the influence of the mixed layer and of the barrier layer. We verified that the apparent phase speed of the thermal signal is nearly independent of depth, 12.6–14.6 cm s^{-1} between 60 and 300 m, which is a useful internal consistency check: the whole thermocline moves coherently, as expected of a baroclinic wave.

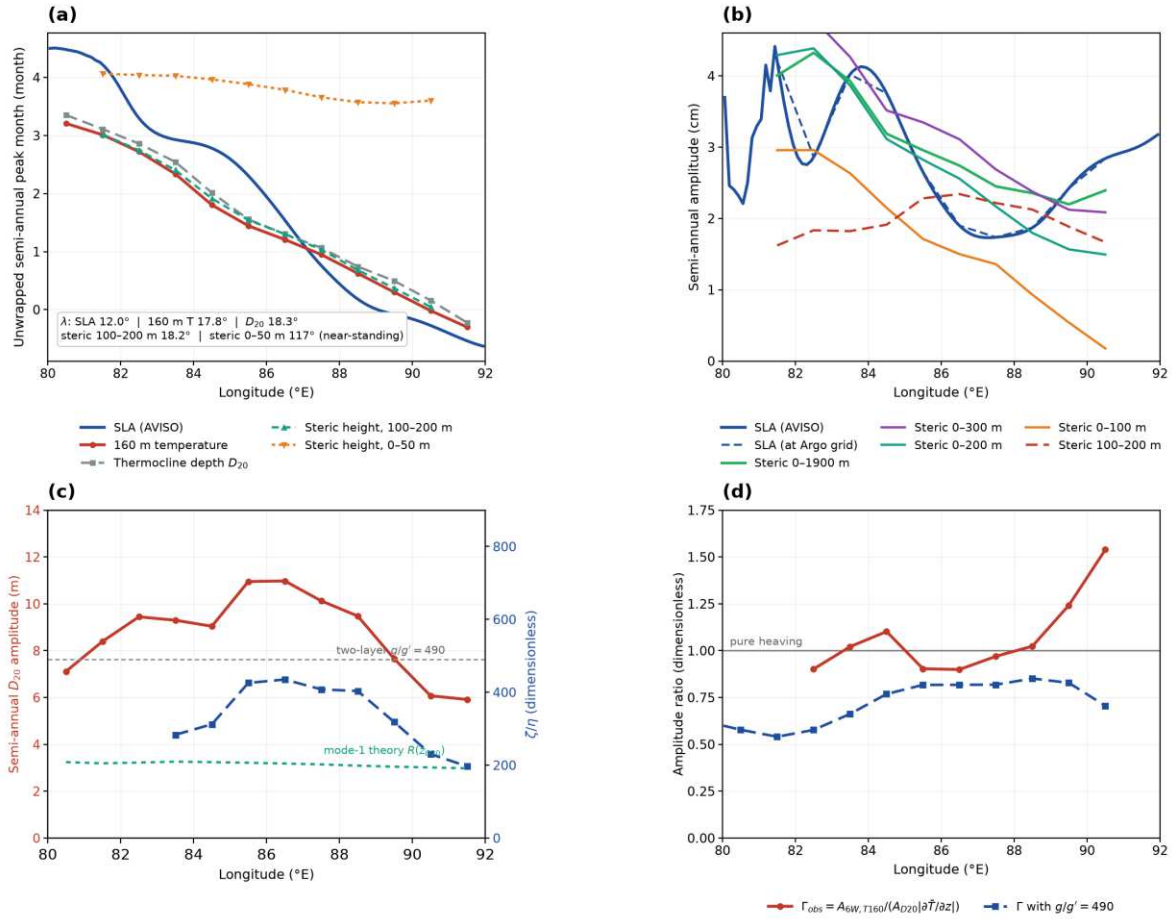


Fig. 4 Mechanism of the decoupling. (a) Unwrapped semiannual peak month versus longitude for SLA, the 160 m temperature, the depth of the 20°C isotherm (D_{20}), and the steric height of the 100–200 m and the 0–50 m layers; the wavelengths quoted in the inset are fitted over the full longitude range shown (80–92°E). (b) Semiannual amplitude of SLA and of the steric height of several layers. (c) Semiannual amplitude of D_{20} (left axis) and the observed displacement-to-height ratio $\zeta/\eta = A_{D20}/A_{6W}(\mathrm{SLA})$ (right axis), together with the two-layer value $g/g' = 490$ and the mode-1 prediction R_1 at the mean D_{20} depth. (d) Amplitude ratio Γ computed with $g/g' = 490$, and $\Gamma_{obs} = A_{6W}(T_{160})/(A_{D20}\cdot|\partial\bar{T}/\partial z|_{160})$ computed from the observed D_{20} displacement and the westward-component amplitude at 160 m; the horizontal line marks pure heaving

3.8 Why the summer–autumn event does not reach the western bay

The semiannual harmonic is by construction symmetric, in the sense that the two events per year must have equal amplitude. The observed monthly anomaly is not. Figures 3b and 5c show that the winter–spring downwelling event grows westward and reaches the western boundary with an amplitude of 1.15–1.24°C at 80.5–82.5°E, whereas the summer–autumn event decays to 0.08°C at 84.5°E and becomes negative, down to −0.57°C, west of 83.5°E. With a threshold of one tenth of the largest event amplitude, the winter–spring event can be traced to 80.5°E and the summer–autumn event only to 85.5°E.

The asymmetry is explained quantitatively by destructive interference with the annual cycle. The two events are separated by six months, so the annual harmonic of period 12 months contributes with equal amplitude and opposite sign to the two event peaks: $A_W = A_6 + C_{12} + r_W$ and $A_S = A_6 - C_{12} + r_S$, where A_6 is the semiannual contribution, which by construction has the same value at both peaks, C_{12} the annual contribution evaluated at the winter–spring peak, and r the contribution of the residual harmonics at each peak, which is small and does not change the sign of either event. For the 160 m temperature band means the ratio C_{12}/A_6 is +0.02 in the east (88–90°E), +0.52 in the

central bay (84–88°E) and +2.42 in the west (80–84°E), reaching +3.34 at 80.5°E (Fig. 2b), while the annual amplitude grows from 0.52°C in the east to 1.00°C in the west and the semiannual contribution at the event peak stays between 0.30 and 0.58°C. The summer–autumn event therefore crosses zero near 84.5°E. The same diagnostic applied to SLA gives a consistent picture, with +4.36 cm for the winter–spring event and −0.14 cm for the summer–autumn event in the western bay, which shows that which of the two events survives is controlled by the phase of the annual harmonic of the respective variable rather than by a weakening of the wave during the second half-cycle. The result is also a warning against interpreting the semiannual harmonic as a description of individual events.

Figure 5 shows this interference directly. At 81.5°E the semiannual reconstruction has a positive peak in April and an equally positive peak in October, whereas the annual reconstruction is +0.93°C in February–April and −0.93°C in August–October, so that it cancels the autumn peak and nearly doubles the spring one (Fig. 5a). At 89.5°E, where the annual contribution at the event peak is only +0.10°C, the two events remain comparable (Fig. 5b). The cancellation is therefore a property of the annual harmonic, whose amplitude grows westward from 0.52°C (88–90°E) to 1.00°C (80–84°E) while the semiannual contribution at the event peak stays within 0.30–0.58°C (Fig. 5d); the two curves cross near 84.5°E, which is where the summer–autumn event changes sign (Fig. 5c).

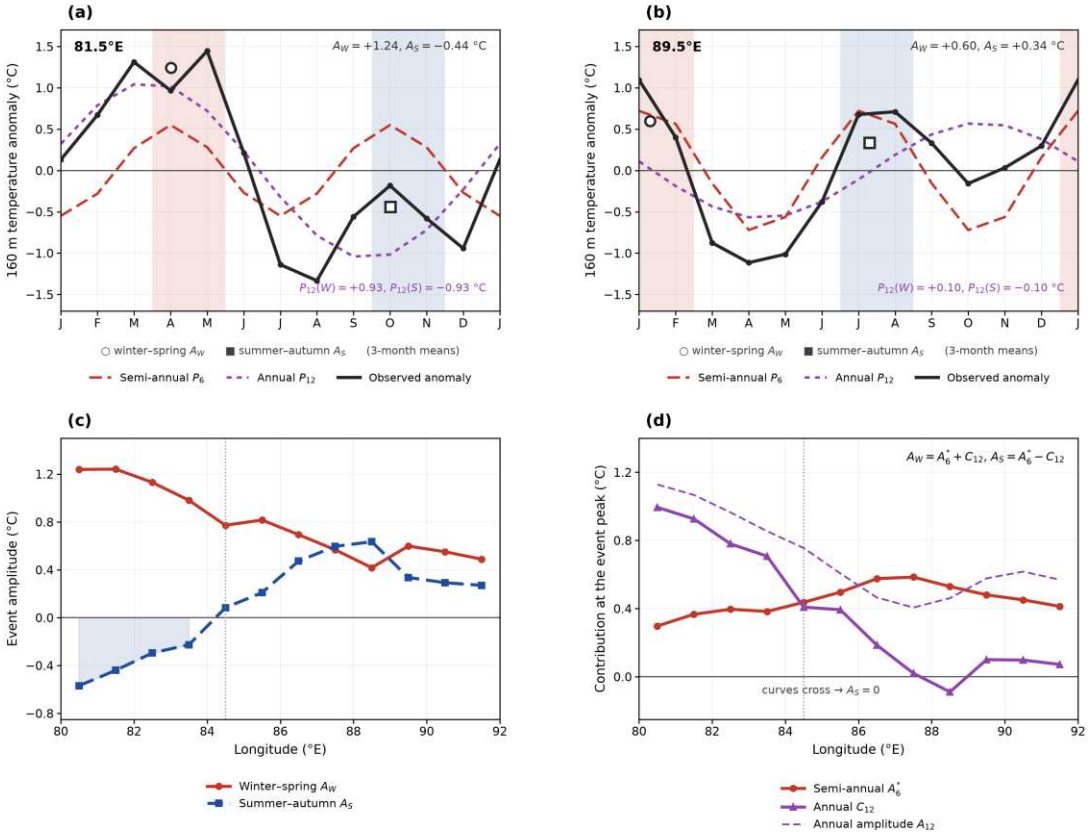


Fig. 5 Destructive interference with the annual cycle explains why the summer–autumn event does not reach the western bay. (a) Monthly climatological 160 m temperature anomaly in the 8–10°N band at 81.5°E (thick line with dots), together with the semiannual (P6) and annual (P12) reconstructions; the shaded bands are the three-month windows centred on the two event peaks, and the open circle and square are the corresponding window means A_W and A_S. (b) Same at 89.5°E. (c) Winter–spring (A_W) and summer–autumn (A_S) event amplitudes versus longitude; the shaded area marks negative A_S and the dotted line the zero crossing near 84.5°E. (d) Semiannual contribution A_6*, annual contribution C_{12} and annual amplitude A_{12} at the event peak versus longitude; the curves cross where $A_S = 0$

4 Discussion

4.1 Two expressions, two vertical sampling operators

The central result of this study is that the altimetric and subsurface thermal expressions of the semiannual wave in the Bay of Bengal are not interchangeable, and that only one of them measures the wave cleanly. It is worth stating precisely what is and what is not claimed. We do not claim that two independent waves of the same period coexist in the band. We claim that the two windows do not return the same wavenumber. The subsurface thermal expression, the 20°C isotherm depth and the 100–300 m steric height all return a wavenumber near 0.35 rad deg^{-1}, that is a wavelength of 18.0–18.3° and a speed of 12.6–12.9 cm s^{-1}, with explained variances above 0.96, whereas the altimetric expression returns k = 0.534 rad deg^{-1} (11.8°, 8.3 cm s^{-1}); the two also differ in phase by up to 1.1 month, which is 18% of the wave period. Table 1 summarizes the fitted wavelengths, speeds and explained variances of all quantities considered. Since a single linear wave can have only one wavenumber, at most one of these numbers is the wavenumber of the wave, and the mode calculation of Section 3.6 identifies the subsurface value as the correct one. The layer-wise steric decomposition shows why the surface differs: a large quasi-standing part of the semiannual steric height is generated in the upper 100 m, whereas the propagating signal is generated by the thermocline displacement at 100–300 m. Any surface measurement integrates the two, whereas a temperature measurement at 160 m responds essentially to the latter alone.

This has an immediate methodological consequence for the BoB, and probably for other freshwater-influenced tropical basins. Studies that infer the properties of the semiannual Rossby wave from altimetry alone will underestimate its phase speed by about one third and misplace its phase by up to one month, and short-wavelength features of the SLA field such as the amplitude minimum at 88–89°E may be artifacts of the interference rather than properties of the wave itself. Altimetry is not wrong, in that the SLA does contain the wave, but it is not a pure measure of it.

Table 1 Zonal wavelength λ, westward phase speed c and fraction of variance explained by a single zonal plane wave fitted to the complex semiannual amplitude over 81.5–90.5°E. The last two rows are semiannual first-baroclinic-mode predictions at 9°N from the dispersion relation with l = 0 and with a 3° meridional confinement (L_y = 3°). The subsurface quantities share a common wavenumber to within about 10%; the altimetric SLA does not

Quantity	Wavelength	Speed (cm s^{-1})	Explained variance
SLA (altimetry)	11.8°	8.3	0.87
T (160 m)	18.0°	12.6	0.97
D_{20} (20 °C isotherm depth)	18.3°	12.9	–
Steric height 100–200 m	18.0°	12.8	0.98
Steric height 100–300 m	18.0°	12.8	0.98
Steric height 100–1900 m	19.7°	13.9	0.99
Steric height 0–1900 m	15.6°	11.0	–
Steric height 0–100 m	43–52°	–	0.77
Steric height 0–50 m	≈90°	–	0.96
Mode 1, l = 0 (theory)	≈37° (4100 km)	26.0	–
Mode 1, L_y = 3° (theory)	≈17.6° (1940 km)	12.3	–

Figure 6 makes the single-wave reading explicit. For each quantity we scan the wavelength of a single zonal plane wave fitted to the complex semiannual amplitude over 81.5–90.5°E and record the fraction of variance explained by the best-fitting wave of that wavelength. The 160 m temperature, the 100–300 m steric height and the 100–1900 m steric height all reach their maximum between 17.9° and 19.7° with 0.97–0.99 of the variance explained, so they form a single family with one wavenumber, $k \approx 0.32–0.35$ rad deg^{-1}, equivalent to a wavelength of about 18° and a speed of 12.6–13.9 cm s^{-1} (Table 1; Fig. 6). The SLA peaks at 11.8° with only 0.87 of the variance explained and lies outside that family, and the total 0–1900 m steric height sits between the two at 15.6°. The quasi-standing upper layer is visible at the other end of the axis, where the 0–50 m steric height reaches its maximum at about 90° and the 0–100 m integral at 43°. The two observational windows are therefore not equivalent observations of one and the same wave; only the subsurface thermal expression recovers a single freely propagating first-mode Rossby wave.

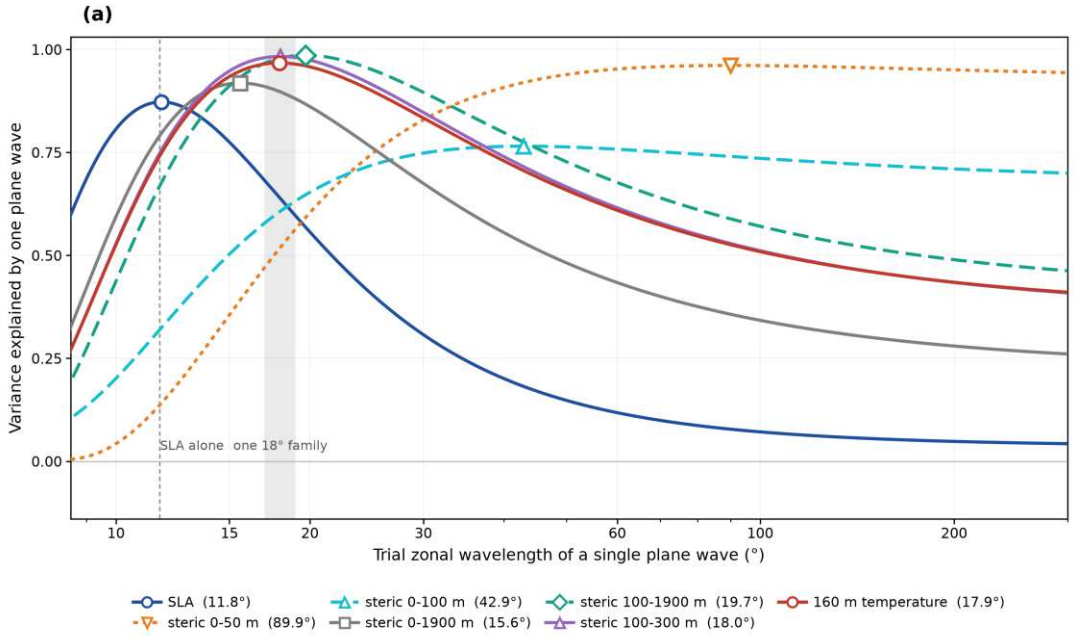


Fig. 6 The two observational windows are not equivalent observations of one wave. Variance explained by a single zonal plane wave fitted to the complex semiannual amplitude over 81.5–90.5°E, as a function of the trial wavelength; the optimum wavelength of each quantity is given in the legend. The subsurface quantities (160 m temperature, 100–300 m and 100–1900 m steric height) form one family between 17.9° and 19.7°, the total 0–1900 m steric height takes an intermediate value of 15.6°, the upper-layer integrals stand aside at 43° and 90°, and SLA is alone at 11.8°

4.2 What is the quasi-standing upper-layer signal?

Our data allow the signal to be characterized but not attributed unambiguously. It is concentrated in the upper 100 m, its zonal phase varies by less than half a month across the basin, and its amplitude decreases eastward from 1.6–1.7 cm near 82°E to about 0.7 cm at 90.5°E. Three candidate processes are consistent with this signature. First, local Ekman pumping by the semiannual wind stress curl, whose spatial pattern is fixed by the geometry of the basin and of the coastline and which therefore produces a phase-locked, quasi-standing response. Second, haline steric changes associated with the monsoon freshwater cycle: the BoB receives freshwater of order 1 m yr^{-1}, and a salinity change of 0.5 in a 50 m layer produces about 2 cm of steric height, comparable to the observed SLA amplitude, with the monsoon river discharge peaking in August–September so that the surface salinity minimum is seasonally locked to the monsoon rather than propagating freely. Third, a remotely forced component generated at the eastern boundary

or at the equator, which would enter the bay with a different zonal wavenumber. Distinguishing among these possibilities requires either a modelling study with a wind-forcing decomposition or salinity observations at a higher vertical resolution than the 1° Argo grid provides, and the question is left open.

The seasonality of the upper-layer contribution coincides with that of the semiannual SLA: the 0–50 m steric anomaly peaks in late April to early May at both longitudes shown, whereas the arriving thermocline signal peaks in February–April in the west and in January in the east (Fig. 7c). The two contributions are therefore partly in phase at the western boundary, which is consistent with the observed maximum of the SLA amplitude in the western bay.

Figure 7 quantifies the structure of the upper-layer signal and the along-path speed. Mapped over the bay, the local apparent wavelength of the semiannual SLA (Fig. 7a) falls to 11.0° in the middle of the coherent band, against 19.0° for the 160 m temperature field at the same longitude (Fig. 7b); both values are consistent with the single plane-wave wavelengths fitted over the whole band, 11.8° and 18.0°. The first baroclinic mode confined to a 3°-wide band returns 16.7–17.6° and 11.9–12.6 cm s^{-1}, in agreement with the thermal field, whereas the classical two-dimensional first mode would give 34.3–38.1° and 24.6–27.3 cm s^{-1}. The seasonal cycles of the two steric layers (Fig. 7c) show that the difference is a phase behavior rather than an amplitude effect: the 0–50 m crest stays in late April to early May across the band, its month changing by only half a month between 82.5 and 89.5°E, whereas the 100–300 m crest moves from mid-March to early January over the same distance, in step with the subsurface thermal field.

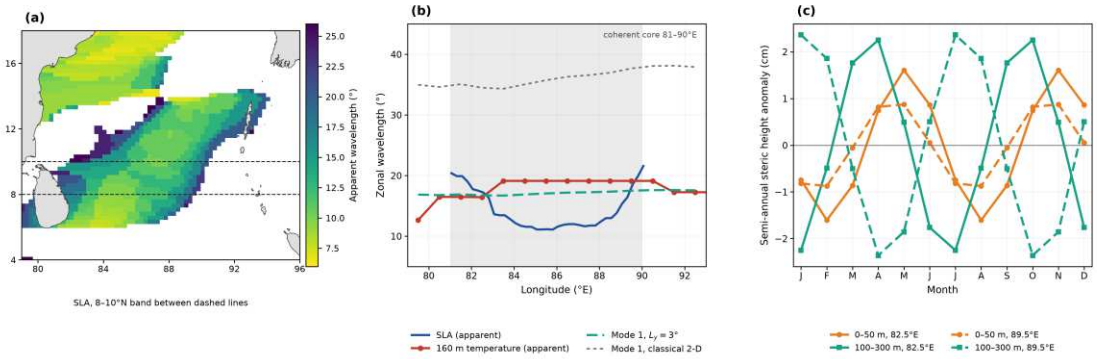


Fig. 7 The quasi-standing upper-layer contribution and the along-path wave speed. (a) Apparent zonal wavelength of the semiannual SLA westward component over the bay; the 8–10°N band is marked by dashed lines. (b) Zonal wavelength along 8–10°N for the SLA (apparent), the 160 m temperature (apparent), the first baroclinic mode confined to a 3°-wide band and the classical two-dimensional first mode; the shaded band is the coherent core, 81–90°E. (c) Semiannual steric height anomaly versus month for the 0–50 m and 100–300 m layers at 82.5°E (solid) and 89.5°E (dashed): the upper-layer crest stays in late April to early May at both longitudes, whereas the thermocline crest moves from mid-March to early January

4.3 Why the stratification does not explain the along-path speed variation

The along-path variation of the apparent wave speed might be attributed to a spatial variation of the deformation radius, since the Bay of Bengal is strongly stratified in the north and less so in the south and the classical long-wave speed βL_d^2 depends quadratically on L_d. Our calculation excludes this explanation for the band studied here: the first-mode deformation radius changes by only 4% between 80.5 and 92.5°E, giving a 9% change in the predicted speed, whereas the fitted apparent speed of SLA varies by nearly a factor of two. The observed variation is instead a superposition of two effects: interference with the quasi-standing component, and the breakdown of the wave

interpretation at the edges of the coherent band, where the direction purity falls below 0.65. When these are removed, the thermocline-based speed is uniform along the path to within 15%, and the wave field in the 8–10°N band is described by a single mode-1 wave with little horizontal variation of the background state.

Our estimate of the semiannual wave speed, 12.6–12.9 cm s^{-1} at 9°N, is lower than the speed reported for individual intraseasonal Rossby wave events in the bay near 8°N, which is of order 21 cm s^{-1} (Girishkumar et al. 2011), and lower than the two-dimensional long-wave prediction of 26 cm s^{-1}. We attribute the difference to the meridional confinement of the semiannual wave: the climatological semiannual wind and buoyancy forcing is itself banded, so the wave it generates is confined to a narrow latitudinal band and its speed is reduced by the l^2 term. Individual events, generated by less banded forcing, are correspondingly less confined and faster. This is a testable prediction: a wave-speed estimate restricted to the 8–10°N band should be systematically lower than one taken over the whole basin.

4.4 Climatic significance of the climatological wave

The climatological semiannual wave matters because it is a deterministic, phase-locked part of the annual cycle of the bay, because of its timing and because of its amplitude (Xiao et al. 2026). Figure 8 summarizes these consequences. The arrival month of the winter–spring crest for the 160 m temperature field (Fig. 8a) progresses from mid-January at 89.5°E to the first half of April at 80.5°E, so the crest takes about three months to cross the coherent part of the bay. The pointwise geostrophic meridional velocity anomaly reaches 4.2 cm s^{-1} (Fig. 8b), and the semiannual D_{20} anomaly is 5.9–11.0 m with a maximum in March–April (Fig. 8c): the water column is anomalously deep exactly when the crest reaches the western boundary.

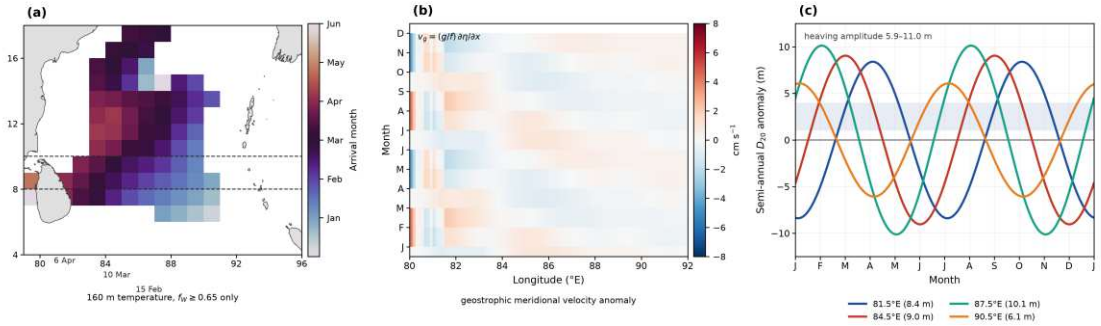


Fig. 8 Climatic significance of the climatological wave. (a) Arrival month of the winter–spring semiannual crest for the 160 m temperature field, shown only where the westward purity $f_W \geq 0.65$; the 8–10°N band is marked by dashed lines and the crest positions at 85.5, 83.5 and 80.5°E are annotated. (b) Geostrophic meridional velocity anomaly $(g/f)\partial\eta/\partial x$ computed from the semiannual SLA field, as a function of longitude and month. (c) Semiannual D_{20} anomaly versus month at four longitudes; the shaded band marks the February–April arrival window

Timing. The westward-propagating crest of the winter–spring downwelling event reaches 85.5°E in mid-February, 83.5°E in early March and 80.5°E in the first half of April. The signal therefore arrives at the western boundary just as the bay enters the pre-monsoon season, when sea surface temperature warms towards its annual maximum and the spring warm pool develops. The spring warm pool has been documented in the central bay at 6–13°N, emerging in early April, peaking in early May and dissipating in early June, and its heat content is dominated by net air–sea heat flux rather than by ocean dynamics (Lin et al. 2024). Our results do not contradict this. They suggest that the role of

the wave is not to supply heat but to set the background stratification: a thermocline deepened by about 10 m and a thickened barrier layer suppress entrainment cooling during the pre-monsoon period and thereby modulate how much of the air–sea heat input is retained in the surface layer. This is the same mechanism that has been invoked for the amplitude of the spring warm pool and for the preconditioning of pre-monsoon cyclones.

Circulation. The zonal phase gradient of the semiannual SLA implies geostrophic meridional velocity anomalies of a few centimetres per second along 8–10°N: the scaling $(g/f)(2\pi/\lambda)A_6$ with A_6 = 3 cm and λ = 11.8° gives about 6 cm s^{-1}, while the pointwise evaluation of $(g/f)\partial\eta/\partial x$ on the observed amplitude and phase field reaches 4.2 cm s^{-1} (Fig. 8b), and the anomalous sea level gradients across the band imply comparable zonal velocities. During the winter–spring event the wave thus reinforces the southward EICC, whose seasonal reversal and eddy-guided structure are well documented from altimetry (Durand et al. 2009), whereas the summer–autumn event acts oppositely. Because the winter–spring event survives to the western boundary and the summer–autumn event does not, the annual net effect of the wave is asymmetric and contributes to the seasonal bias of the western boundary current. The same remote signal has been shown to precondition the bay for cyclone intensification through the freshwater–SSH coupling (Yu and McPhaden 2011).

Temperature and salinity. The thermocline displacement of 5.9–11.0 m is not confined to temperature: because the interior of the bay has a marked subsurface salinity maximum, heaving displaces that maximum by a comparable amount and thereby modulates the density structure of the interior. In combination with the surface freshwater flux, the wave therefore contributes to the maintenance of the barrier layer (Vinayachandran et al. 2002). A related westward salinity signal, associated with Rossby waves at 10 and 15°N, has been shown to modulate the redistribution of freshwater in the eastern and central bay (Chen et al. 2024). Because the salinity structure controls both the barrier layer and the density stratification, and hence the deformation radius and the wave speed, a potential positive feedback between freshwater input and wave propagation deserves dedicated study.

A methodological point about climatological waves. Our analysis also shows that the climatological semiannual harmonic, the standard way of describing the wave, contains information that no single event contains: the two events are unequal in the observations because of the annual harmonic, yet identical in the harmonic decomposition. Statements about the wave and statements about events must therefore be kept separate.

5 Summary and conclusions

Using 22 years of satellite altimetry together with Argo temperature and salinity data, we have examined the climatological semiannual Rossby wave of the Bay of Bengal and the way it appears in two different observational windows. Our conclusions are as follows.

- A coherent semiannual westward wave exists, but only in a narrow band. Direction purity exceeds 0.65 only between about 7 and 11°N, and within that band between 81 and 90°E the semiannual signal is close to a single plane wave, which explains 87% of the variance for SLA and 97% for the 160 m temperature. Equatorward and poleward of the band, and in the upper 50 m, the signal is standing or locally forced.

• The two windows do not return the same wavenumber, and only the subsurface one is the wave. The 160 m temperature, the 20°C isotherm depth and the 100–300 m steric height all return a wavenumber near 0.35 rad deg^{-1}, a wavelength of 18.0–18.3° and a speed of 12.6–12.9 cm s^{-1}, with explained variances above 0.96, whereas SLA returns k = 0.534 rad deg^{-1} (11.8°, 8.3 cm s^{-1}) and drifts in phase from +0.4 month in the east to −1.1 month in the west. Because a single linear wave has a single wavenumber, these are not two coexisting waves of the same period but one wave seen through two different vertical sampling operators, of which only the subsurface one is clean. The 35% difference in apparent wavelength is the kinematic expression of the phase drift.

• The cause is a quasi-standing near-surface steric signal together with a non-steric contribution. The 0–50 m steric height, 1.34 cm or 47% of the SLA amplitude, is quasi-standing with a wavelength near 90°, and the 0–100 m integral, 1.7 cm or 60% of the SLA, has a wavelength of 43–52°, while the 100–300 m layer propagates at 12.8 cm s^{-1}. Removing the upper layer restores a clean 19.7° wave; including it compresses the full 0–1900 m steric wavelength to 15.6° and produces the amplitude minimum and the phase rotation near 88–89°E. The observed SLA wavelength of 11.8° is shorter still, and SLA differs from the 0–1900 m steric height by 52% of its complex amplitude, so a non-steric contribution is also present; the attribution of that residue is treated as an open question.

• The amplitude decoupling implied by a fixed conversion factor is largely a normalization artifact. The two-layer value $g/g' = 490$ exceeds both the observed displacement-to-height ratio, 370, and the mode-1 prediction, 165. Using the observed D_{20} displacement and the westward-component amplitude at 160 m, the temperature anomaly is consistent with heaving, with $\Gamma_{obs} = 1.01$ and a range of 0.90–1.54. The genuine decoupling is therefore kinematic: the two expressions of the wave do not share a single wavenumber.

• First-mode theory with meridional confinement reproduces the observed speed. The Argo stratification gives $c_1 = 2.42$–2.54 m s^{-1}, equivalent to $L_{d1} = 106$–111 km. The classical two-dimensional semiannual speed is 26 cm s^{-1}, twice the observed value; confining the wave to a 3°-wide band reduces it to 12.3 cm s^{-1}, matching the observed 12.6–12.9 cm s^{-1}. The along-path variation of the apparent speed is caused not by the 4% variation of L_{d1} but by interference and by the non-wave nature of the signal outside the coherent band.

• The summer–autumn event is cancelled by the annual cycle in the western bay. The ratio C_{12}/A_6 for the 160 m temperature is +0.02 in the east, +0.52 in the central bay and +2.42 in the west. Consequently the winter–spring downwelling event reaches 80.5°E with an amplitude of 1.2°C, or 4.4 cm in SLA, whereas the summer–autumn event vanishes near 84.5°E. Which event survives is controlled by the phase of the annual harmonic rather than by a weakening of the wave.

• Climatic implications. The surviving winter–spring crest reaches the western bay in February–April, deepens the thermocline by about 10 m, and implies geostrophic meridional velocity anomalies of order 4–6 cm s^{-1} (Fig. 8b); because the summer–autumn event is absent, the annual-mean effect of the wave on the western boundary layer is not symmetric. The resulting background stratification and barrier-layer thickness modulate the retention of the spring air–sea heat input and the preconditioning of the monsoon onset and of pre-monsoon cyclones.

- Methodological recommendation. Altimetry alone is not a reliable measure of the semiannual Rossby wave in a freshwater-influenced tropical basin. Wave speed and phase inferred from SLA should be cross-checked against the thermocline displacement inferred from subsurface temperature or from isotherm depth.

Author contributions

Fuwen Qiu conceived and designed the study, developed the local plane-wave projection, the layer-wise steric decomposition and the normal-mode diagnostics, performed all of the computations, prepared the figures and wrote the first draft of the manuscript. Shucai Wang and Yun Qiu contributed to the interpretation of the results and to the framing of the discussion. Junpeng Zhang assisted with the processing of the altimetry data and commented on the manuscript. All authors read and approved the final manuscript.

Acknowledgements

This work was funded by the National Natural Science Foundation of China (42130406), the Scientific Research Foundation of the Third Institute of Oceanography, MNR (grant numbers 2026058, 2026048, 2023018 and 2023014), and the Global Change and Air-Sea Interaction II Program (GASI-04-WLHY-03; GASI-01-SIND-STwin). The authors thank the International Argo Program and the national programmes that contribute to it, the Copernicus Marine Environment Monitoring Service, and the Natural Earth project for making their data products freely available.

Data availability

The DUACS L4 multimission sea level product is available from CMEMS (https://marine.copernicus.eu; Pujol et al. 2016); the gridded Argo temperature and salinity product from the Argo Global Data Assembly Centre (https://doi.org/10.17882/42182; Argo 2000); and the Natural Earth 1:10 m land polygons from https://www.naturalearthdata.com.

Code availability

All of the analysis was carried out with Python and MATLAB scripts written by the first author. The codes that perform the plane-wave projection, the layer-wise steric decomposition, the vertical normal-mode solutions and the production of the figures, together with a description of the input files and of the order in which the scripts are run, are available from the corresponding author on reasonable request.

Declarations

Competing interests The authors have no competing interests to declare that are relevant to the content of this article.

References

Argo (2000) Argo float data and metadata from Global Data Assembly Centre (Argo GDAC). SEANOE. https://doi.org/10.17882/42182

Chelton DB, Schlax MG (1996) Global observations of oceanic Rossby waves. Science 272(5259):234–238. https://doi.org/10.1126/science.272.5259.234

Chelton DB, deSzoeke RA, Schlax MG, El Naggar K, Siwertz N (1998) Geographical variability of the first baroclinic Rossby radius of deformation. J Phys Oceanogr 28(3):433–460. https://doi.org/10.1175/1520-0485(1998)028<0433:GVOTFB>2.0.CO;2

Chen G, Li Y, Xie Q, Wang D (2018) Origins of eddy kinetic energy in the Bay of Bengal. J Geophys Res Oceans 123(3):2097–2115. https://doi.org/10.1002/2017JC013455

Chen S, Qiu F, Jing C, Qiu Y, Zhang J (2024) Unraveling the influence of equatorial waves on post-monsoon sea surface salinity anomalies in the Bay of Bengal. Remote Sens 16(8):1348. https://doi.org/10.3390/rs16081348

Chen T, Wang D, Huang K, Peng Q (2025) Distinct phase-locked local and remote forcing deepens the summer thermocline in the southern Bay of Bengal. Ocean Dyn 75(11):95. https://doi.org/10.1007/s10236-025-01741-z

Durand F, Shankar D, Birol F, Shenoi SSC (2009) Spatiotemporal structure of the East India Coastal Current from satellite altimetry. J Geophys Res Oceans 114(C2):C02013. https://doi.org/10.1029/2008JC004807

Gill AE (1982) Atmosphere–ocean dynamics. Academic Press, New York

Girishkumar MS, Ravichandran M, McPhaden MJ, Rao RR (2011) Intraseasonal variability in barrier layer thickness in the south central Bay of Bengal. J Geophys Res Oceans 116(C3):C03009. https://doi.org/10.1029/2010JC006657

Goswami BN, Rao SA, Sengupta D, Chowdary JS (2016) Monsoons to mixing in the Bay of Bengal: multiscale air-sea interactions and monsoon predictability. Oceanography 29(2):18–27. https://doi.org/10.5670/oceanog.2016.35

Han W, McCreary JP (2001) Modeling salinity distributions in the Indian Ocean. J Geophys Res Oceans 106(C1):859–877. https://doi.org/10.1029/2000JC000316

Killworth PD, Chelton DB, de Szoeke RA (1997) The speed of observed and theoretical long extratropical planetary waves. J Phys Oceanogr 27(9):1946–1966. https://doi.org/10.1175/1520-0485(1997)027<1946:TSOOAT>2.0.CO;2

Lin W, Qiu Y, Ni X, Lin X, Liu T (2024) Evolution characteristics and mechanisms of the spring warm pool in the Bay of Bengal. Front Mar Sci 11:1425722. https://doi.org/10.3389/fmars.2024.1425722

Lin X, Yang J, Wu D, Zhai P (2008) Explaining the global distribution of peak-spectrum variability of sea surface height. Geophys Res Lett 35(14):L14602. https://doi.org/10.1029/2008GL034312

Mackenzie KV (1981) Nine-term equation for sound speed in the oceans. J Acoust Soc Am 70(3):807–812. https://doi.org/10.1121/1.386920

Masumoto Y, Meyers G (1998) Forced Rossby waves in the southern tropical Indian Ocean. J Geophys Res Oceans 103(C12):27589–27602. https://doi.org/10.1029/98JC02546

McCreary JP, Han W, Shankar D, Shetye SR (1996) Dynamics of the East India Coastal Current: 2. Numerical solutions. J Geophys Res Oceans 101(C6):13993–14010. https://doi.org/10.1029/96JC00560

Pang S, Wang X, Foltz GR, Fan K (2024) Contribution of the winter salinity barrier layer to summer ocean–atmosphere variability in the Bay of Bengal. Acta Oceanol Sin 43(9):35–53. https://doi.org/10.1007/s13131-024-2360-5

Pujol MI, Faugère Y, Taburet G, Dupuy S, Pelloquin C, Ablain M, Picot N (2016) DUACS DT2014: the new multi-mission altimeter data set reprocessed over 20 years. Ocean Sci 12(5):1067–1090. https://doi.org/10.5194/os-12-1067-2016

Roemmich D, Gilson J (2009) The 2004–2008 mean and annual cycle of temperature, salinity, and steric height in the global ocean from the Argo Program. Prog Oceanogr 82(2):81–100. https://doi.org/10.1016/j.pocean.2009.03.004

Schott FA, Xie SP, McCreary JP (2009) Indian Ocean circulation and climate variability. Rev Geophys 47(1):RG1002. https://doi.org/10.1029/2007RG000245

Shankar D, Vinayachandran PN, Unnikrishnan AS (2002) The monsoon currents in the north Indian Ocean. Prog Oceanogr 52(1):63–120. https://doi.org/10.1016/S0079-6611(02)00024-1

Shetye SR, Gouveia AD, Shenoi SSC, Sundar D, Michael GS, Nampoothiri G (1993) The western boundary current of the seasonal subtropical gyre in the Bay of Bengal. J Geophys Res Oceans 98(C1):945–954. https://doi.org/10.1029/92JC02070

Somayajulu YK, Murty VSN, Sarma YVB (2003) Seasonal and inter-annual variability of surface circulation in the Bay of Bengal from TOPEX/Poseidon altimetry. Deep Sea Res II 50(5):867–880. https://doi.org/10.1016/S0967-0645(02)00610-0

UNESCO (1981) Tenth report of the joint panel on oceanographic tables and standards. UNESCO Technical Papers in Marine Science 36. UNESCO, Paris

Vinayachandran PN, Murty VSN, Ramesh Babu V (2002) Observations of barrier layer formation in the Bay of Bengal during summer monsoon. J Geophys Res Oceans 107(C12):8018. https://doi.org/10.1029/2001JC000831

Xiao H, Wang L, Qu H, Song Y (2026) Quantitative analysis of sea surface temperature warming prior to the summer monsoon onset over the Bay of Bengal. J Sea Res 210:102681. https://doi.org/10.1016/j.seares.2026.102681

Yu L, McPhaden MJ (2011) Ocean preconditioning of Cyclone Nargis in the Bay of Bengal: interaction between Rossby waves, surface fresh waters, and sea surface temperatures. J Phys Oceanogr 41(9):1741–1755. https://doi.org/10.1175/2011JPO4437.1